

Design, implementation, and characterization of a hybrid optical interconnect for a four-stage free-space optical backplane demonstrator

Yongsheng Liu, Brian Robertson, Guillaume C. Boisset, Michael H. Ayliffe, Rajiv Iyer, and David V. Plant

A four-stage unidirectional ring free-space optical interconnect system was designed, analyzed, implemented, and characterized. The optical system was used within a complementary metal-oxide semiconductor–self-electro-optic-effect-device-based optical backplane demonstrator that was designed to fit into a standard VME chassis. This optical interconnect was a hybrid microlens–macrolens system, in which the microlens relays were arranged in a maximum lens-to-waist configuration to route the optical beams from the optical power supply to the transceiver arrays, while the macrolens optical relays were arranged in a telecentric configuration to route optical signal beams from stage to stage. The following aspects of the optical system design are discussed: the optical parameters for the hybrid optical system, the image mapping of the two-dimensional array of optical beams from stage to stage, the alignment tolerance of the hybrid relay system, and the power budget of the overall optical interconnect. The implementation of the optical system, including the characterization of optical components, subsystem prealignment, and final system assembly, is presented. The two-dimensional array of beams for the stage-to-stage interconnect was adjusted with a rotational error of $<0.05^\circ$ and a lateral offset error of $<3.5\ \mu\text{m}$. The measured throughput is in good agreement with the lower-bound predictions obtained in the theoretical results, with an optical power throughput of $-20.2\ \text{dB}$ from the fiber input of the optical power supply to the modulator array and $-25.5\ \text{dB}$ from the fiber input to the detector plane. © 1998 Optical Society of America

OCIS codes: 200.2610, 200.4650.

1. Introduction

Free-space optical interconnects offer several potential advantages for implementing highly parallel networks with large data bandwidths.¹ These advantages include high bandwidth, low skew and cross talk, small volume, high connection density, and lower power consumption. Thus optically interconnecting electronic components may overcome the present limitations of electronic interconnects in a simple and cost-effective

manner. Several optical systems have been demonstrated.^{2–10} However, most of the previous systems were built-in stand-alone custom environments such as custom-machined slot-based baseplates or a custom chassis. To design a free-space optical interconnect system that can be integrated into current electronic systems, the optical system designers, along with the optical packaging designers, must respect the spatial constraints imposed by electronics. Other requirements such as scalability, complexity, efficiency, and alignability also have to be considered.

Intelligent optical backplanes that merge complementary metal-oxide semiconductor (CMOS) processing with free-space optical interconnects between printed circuit boards (PCB's) were proposed in Ref. 11. These systems differ from previous optical backplanes in that they support intelligence directly in the optoelectronic interconnect. This intelligence allows for optical packet-address recognition, packet filtering and extraction, and other forms of optical

When this research was performed the authors were with the Department of Electrical Engineering, McGill University, McConnell Engineering Building, 3480 University Street, Montreal, Quebec, Canada H3A 2A7. Y. S. Liu is now with Quinta Corporation, 1870 Lundy Avenue, San Jose, California 95131.

Received 26 August 1997; revised manuscript received 15 January 1998.

0003-6935/98/02895-20\$15.00/0

© 1998 Optical Society of America

data processing. The intelligence coupled with the high optical bandwidths yields capabilities that were not possible with previous optical systems. The architectural design and the capabilities of intelligent optical backplanes are described in Ref. 11. Challenges involved with filtering large amounts of optical data clocked at high rates are described in Ref. 12. Performance analyses for one-dimensional intelligent optical backplanes in an industry-standard rack and for higher-dimensional optical systems that could be used to interconnect electronic PCB's in an industry-standard cabinet can be found in Ref. 13.

Given an optical design problem, a unique type of optical interconnect is generally best suited.¹⁴ An optical interconnect system based on macrolenses (conventional lenses) has the advantages of simplicity, ease of alignment, and ease of assembly. However, the optical system tends to be bulky, and the required performance of the lenses tends to be high. In contrast, an optical system based on microlens arrays is compact and scalable. Such a system is suitable for interconnecting large arrays of electronic devices over short distances. The main disadvantage of microlens systems is their poor alignment tolerances. A hybrid optical system that uses microlenses and macrolenses combines the advantages of both types of interconnects. It also provides more freedom for choosing optical parameters (such as various combinations of focal lengths) when an optical system is being designed. Therefore a hybrid system has greater flexibility but is usually more complex since more optical components are involved.

This paper describes the design, implementation, and characterization of the optical system for a CMOS-self-electro-optic-device-based (CMOS-SEED-based) four-stage unidirectional ring free-space optical backplane demonstrator.^{11,15} This optical system is a hybrid microlens-macrolens type of interconnect. Microlens arrays were used to route optical beams within a stage, while macrolenses were used to relay optical beams between stages. The advantages of such an arrangement are that the microlens optical interconnect relieved the constraints imposed by typical conventional macro-optic implementations. As a result, the inherent problems associated with the limited numerical aperture and small field of view of simple macrolens relays were no longer significant factors in the microlens relays.¹⁶⁻²¹ The optical interconnect is unaffected by the angular dependence of polarizing beam splitters (PBS's). Thus the microlens relays were simple and compact with low component count, minimal latency, and high scalability. At the same time, the macrolens relay between stages allowed the separation of the PCB's to be close to the conventional VME standard pitch (25-30 mm). The macrolens optical relay also provided space for the illumination and imaging system, which was essential for optical system assembly.

This paper provides a description of the design, implementation, and characterization of the optical interconnect used in this backplane demonstrator. In Section 2 an overview of the demonstration system

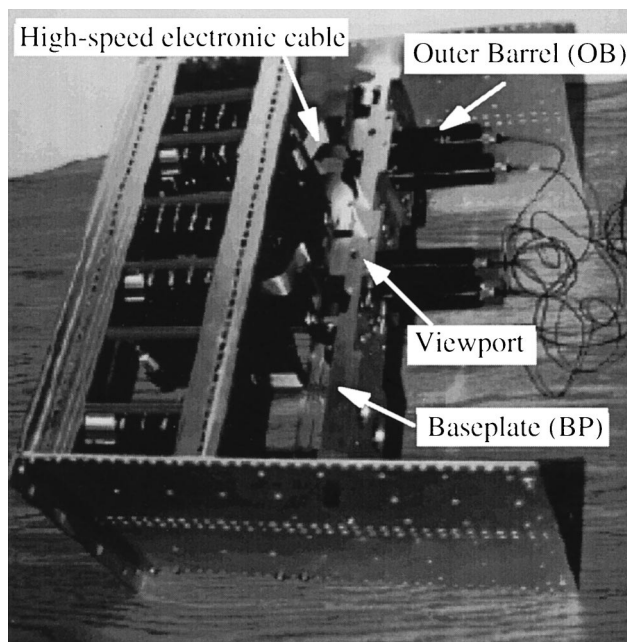


Fig. 1. Optical backplane system in a 6U VME chassis.

is presented. In Section 3 the following are discussed: the optical system design, which includes the alignment tolerances of the optical interconnect, and the image mapping associated with the two-dimensional (2-D) beam array in the stage-to-stage optical interconnect. Section 4 describes the characterization of the optical components used in the demonstrator, including the diffractive microlens arrays and the PBS and quarter-wave plate (QWP) assembly (PBS+QWP assembly). Section 5 describes the prealignment and assembly of subsystems. Section 6 discusses the problems involved in the optical system assembly. Section 7 presents the experimental performance of the optical system and compares those measured results with predicted performance. Finally, Section 8 concludes the paper with comments on system performance.

2. Optical Backplane System Overview

The optical backplane was designed to fit into a standard 19-in. (48.26-cm) 6U VME backplane chassis, and it occupied the rear portion of the chassis, as shown in Fig. 1. The CMOS-SEED optoelectronic devices were surface mounted directly onto four custom-designed printed circuit daughterboards²² (DB's) that were connected to the four PCB's at the front portion of the chassis by means of four high-speed electronic ribbon cables (3 in. long). This approach allowed for mechanically decoupling the optical system from the electronic design, while still preserving the bandwidth between the PCB's and the photonic backplane.⁹ Thus an end user of the VME backplane would see the same functionality as an electronic backplane, but with a higher interconnection bandwidth. It is also interesting to note the three-dimensional nature of the system. As shown in Fig. 1, the outer barrels are mounted or-

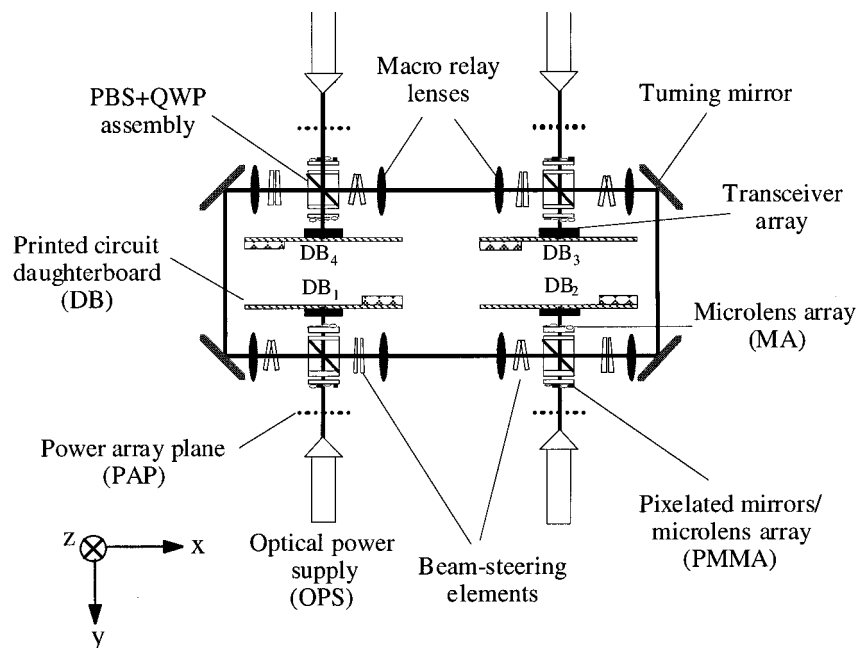


Fig. 2. Schematic of the unfolded overall optical system.

thogonally with respect to the baseplate. This three-dimensional arrangement was required to fit the system in the chassis.¹⁵ A schematic of the unfolded optical layout of the system is shown in Fig. 2. A hybrid microlens-macrolens optical system was chosen since it provided a simple and efficient way to route the optical signal beams and was also flexible enough for adjusting the stage-to-stage separation to the required value. This optical system can be divided into two subsystems: the optical power supply (OPS) that provided a set of 4×8 arrays of beams and the optical relay system. In the optical relay system the microlens relays routed the arrays of optical beams generated from the OPS to the transceiver arrays; the macrolens relay system relayed the

optical beams from stage to stage. Four turning mirrors were used to close the loop of the unidirectional optical ring.

The CMOS-SEED transceiver array was arranged in an 8×8 grid, with a 4×8 array of modulators and a 4×8 array of detectors horizontally offset by $125 \mu\text{m}$. The pitch of the transceiver array was $125 \mu\text{m}$ in both the horizontal and the vertical directions. The optical aperture (window) of each modulator and detector was $20 \mu\text{m} \times 20 \mu\text{m}$.

A. Optical Power Supply

The role of the OPS is to generate a 4×8 array (plus eight alignment beams) of cw beams at the power array plane (PAP). This plane corresponds to the loca-

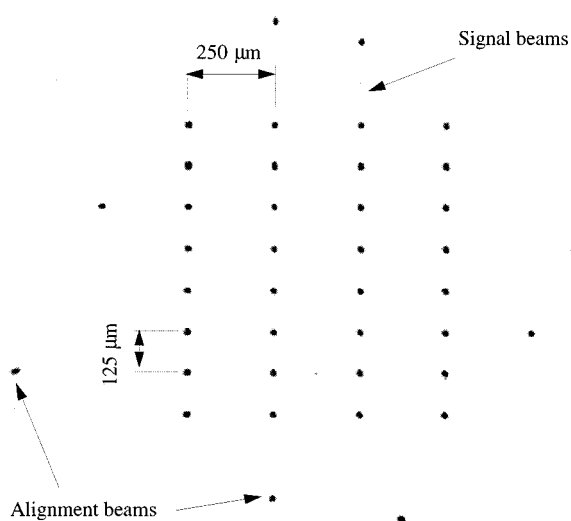


Fig. 3. Frame grab of the spot array at the PAP.

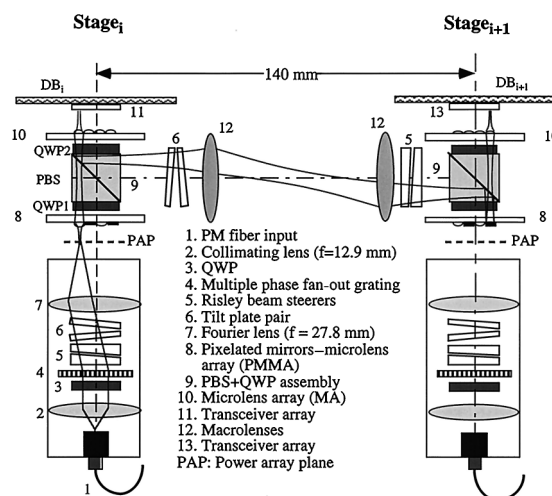


Fig. 4. Stage-to-stage optical relay system.

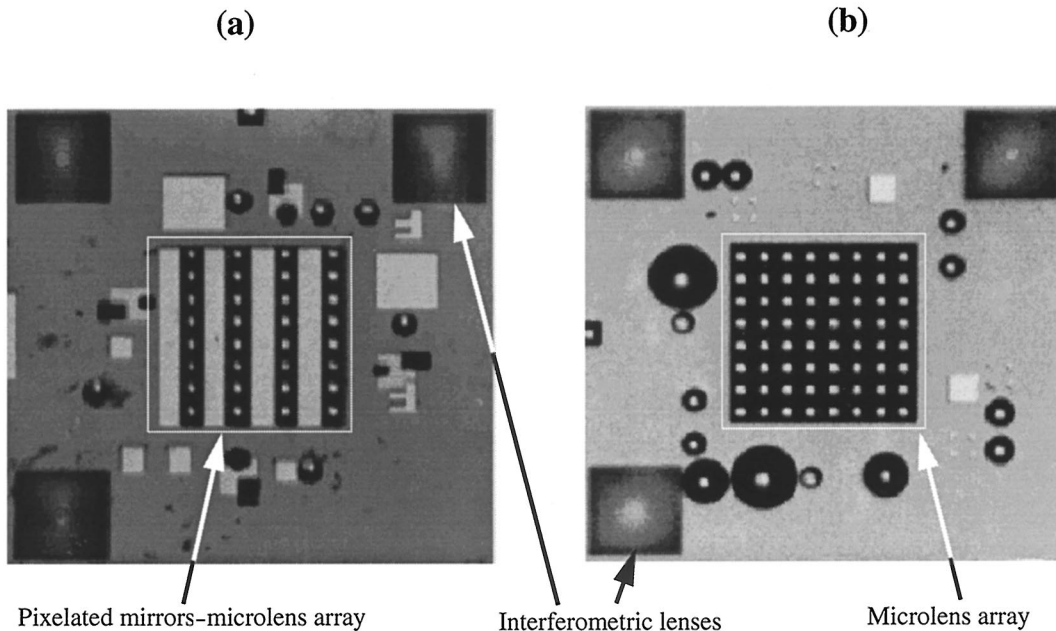


Fig. 5. (a) PMMA. (b) MA. The pixelated mirrors and the microlenses used in the hybrid optical interconnect are shown in the boxed areas.

tion where the minimum spot sizes of the beams occurred. Figure 3 shows a frame-grabbed image of a spot array at a PAP. The input of the OPS was provided from a single-mode polarization-maintaining fiber. The detailed design and characterization of the OPS can be found in Ref. 23 and thus is not covered in detail here.

B. Optical Relay System

The hybrid optical relay system was designed as follows. Symmetric microlens relays (in a maximum lens-to-waist configuration) were used to relay the optical beams from OPS modules to the modulator arrays and to route the modulated signal beams from previous stages to the detector arrays. The macrolens relays (in a telecentric configuration) were used to relay optical signal beams from stage to stage. The details of a stage-to-stage optical interconnect system is shown in Fig. 4. At stage_{*i*}, the circularly polarized array of beams generated by the OPS was first collimated (i.e., the beam was minimum divergent) by the microlens array (MA) of the pixelated mirrors-microlens array (PMMA). The light passed through the first QWP (QWP1) and became *p* polarized. After passing through the PBS and the second QWP (QWP2), the array of beams was focused by the second MA (i.e., a beam waist was formed) onto the apertures of the modulator array. The PMMA is a combination of a microlens array and pixelated mirrors. Pictures of the PMMA and the MA are shown in Fig. 5.

The reflected signal beams from the modulator array were recollimated by the MA and changed to *s*-polarized beams after their second pass through QWP2. The *s*-polarized beams were then reflected off the PBS and relayed to the next stage by the

macrolens relay system. The macrolens relay was arranged in a telecentric configuration to maximize the alignment tolerances.

At stage_{*i+1*}, the *s*-polarized beams coming from stage_{*i*} were reflected by the PBS onto the pixelated mirrors of the PMMA. The distance between the second macrolens and the PBS of stage_{*i+1*} was selected such that the reflected beams from the PBS followed an optical path similar to that from the PAP to the modulator array at stage_{*i*}. However, because of the image-rotation effect of the telecentric relay of the macrolens relay (see Subsection 3.B), the relayed beams were laterally shifted 125 μm away from the OPS beams and were thus focused onto the apertures of the detector array. It should be noted that the selected location of the pixelated mirrors was such that the optical signal beams reflecting from those mirrors were still converging. This allowed the integration of the pixelated mirrors and the microlenses onto a single component, the PMMA. In this way, the number of custom components was reduced and the overall system simplified. Moreover, QWP1, PBS, and QWP2 were glued together as one component, which was collectively called the PBS+QWP assembly. This PBS+QWP assembly reduced the reflectivity, simplified the alignment during system assembly, and reduced the optomechanics to a single mount.

The scalability of the optical system is addressed. The number of optical channels is limited by the spatial constraint of the microlens relay (as shown in Subsection 2.A) and the field of view of the macrolens relay. However, the number of stages is not limited by the optics. More optical stages can be added within the four turning mirrors. Therefore the optical system is scalable to multiple stages.

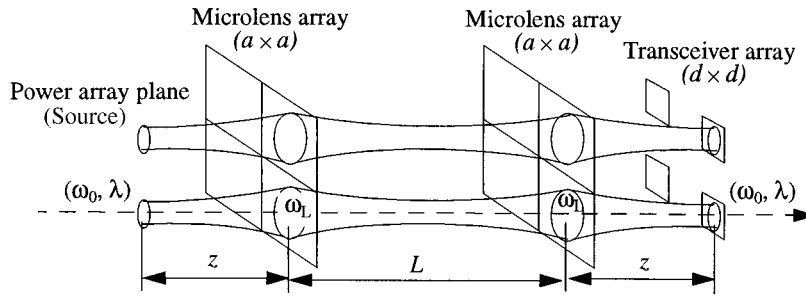


Fig. 6. Schematic of the microlens relay.

C. Optomechanical System

As illustrated in Fig. 1, the optical components were housed in various optomechanical supports. A detailed discussion of the design and the characterization of optomechanical systems can be found in Ref. 24.

For simplicity, we use PMMA_{*i*} to refer to the PMMA and the peripheral alignment features at stage_{*i*}. The same nomenclature is used with all other components.

3. Optical System Design

A. Optical Relay System Design

Optical system design for which a MA is used has been studied for various configurations of microlenses.^{19,25,26} The main design criterion of the optical interconnect system was to maximize the encircled optical power falling onto the apertures of the transceivers. The microlens relay has to route optical beams with high power throughput. The separation between the MA also has to be sufficiently large that the beam-steering and the combination elements (PBS+QWP assemblies) can be housed.

Assuming that the optical beams are Gaussian, for a symmetric microlens relay, as shown in Fig. 6, the optical path length (OPL) between the MA's L can be found in Ref. 27. Let us assume that the aperture of a transceiver is $d \times d$, the pitch of the transceiver array is p , the aperture of a square microlens is $a \times a$, and the focal length of the microlens is f . Because the layout of the CMOS-SEED's on the optoelectronic chip was such that the pitch of the transceiver array was relatively large ($p = 125 \mu\text{m}$), we chose one microlens to support only one transceiver, as opposed to the window-clustering scheme used previously in Ref. 26. Therefore we have $a = p$.

To meet the weak clipping condition (i.e., less than 1% optical power is clipped) by the finite apertures of the optical components^{19,28,29} we must have

$$3\omega_0 \leq d, \quad (1)$$

where ω_0 is the Gaussian beam waist ($1/e^2$ radius). Similarly, to ensure only weak clipping of the beam as it propagates through the microlens interconnect,

we must also restrict the beam radius ω_L at the microlens facets:

$$3\omega_L \leq a. \quad (2)$$

Here ω_L can be related to ω_0 according to standard Gaussian beam-propagation theory:

$$\omega_L = \omega_0 \left[1 + \left(\frac{z}{z_r} \right)^2 \right]^{1/2}, \quad (3)$$

where $z_r = \pi\omega_0^2/\lambda$ is the Rayleigh range of the Gaussian beam, λ is the optical wavelength (850 nm), and z is the distance separating the MA from the transceiver array.

For a microlens relay with a maximum lens-to-waist configuration (i.e., $z = f + z_r$), the OPL between the microlenses is $L = 2f[1 + f/(2z_r)]$.²⁷ When $\omega_0 = 6.5 \mu\text{m}$ and $f = 768 \mu\text{m}$, $L = 5.313 \text{ mm}$, which is sufficient for fitting a compact PBS+QWP assembly. We chose the final separation to be 5.40 mm after considering the weak clipping of the Gaussian beam and optimizing the microlens layout to balance the alignment tolerance. A detailed description of these adjustments is presented in Subsection 3.C.

The PMMA and the MA that are shown in Fig. 5 were custom made. The center portion of the PMMA and the MA contains the microlenses and the pixelated mirrors used in the microlens relays. The pixelated mirrors were fabricated on the same side of the fused-silica substrate as the MA to reduce fabrication complexity. We formed the mirrors by first depositing a thin-film layer of silver [$\sim 500 \text{ \AA}$ (50 nm) thick] on the substrate and then covering it with a gold layer to prevent tarnishing of the silver. The reflectivity of the pixelated mirrors was estimated to be 97.6% on the basis of the parameters of the corresponding bulk materials. The dimensions of the pixelated mirror were $123 \mu\text{m} \times 1000 \mu\text{m}$. The gap between the edge of the pixelated mirror and the column of microlenses was $1 \mu\text{m}$. The microlenses were eight-phase-level diffractive lenses. The apertures of the microlenses were $125 \mu\text{m} \times 125 \mu\text{m}$. The focal length of the diffractive lenses was designed to be $768 \mu\text{m}$ at the 850-nm wavelength. Thus the f -number of the square microlenses was 6.1 (for the largest inscribed circle of the aperture) and 4.3 (for the smallest circumscribed circle of the aperture). The peripheral features on the PMMA and the MA

were used either for prealignment of the microlens relay or for monitoring the long-term stability of the optical interconnect system. Of these features, the two sets of three interferometrical alignment lenses were used to prealign the PMMA to the MA with high alignment accuracy.³⁰ The prealignment results are presented in Subsection 5.B.

The PBS+QWP assembly was custom made and consisted of a 5-mm PBS cube (SF7 glass) with zero-order QWP's. The QWP polymer films were attached directly to the input and the output surfaces of the PBS and then were covered with two 0.82-mm-thick optical windows (Corning, 7905 glass). The orientation of the slow axis of the QWP's with respect to the PBS was $45^\circ \pm 1^\circ$. The overall length of the PBS+QWP assembly was 6.64 mm. All four entrance and exit surfaces of the assembly were anti-reflection (AR) coated for maximum transmission at the 850-nm wavelength.

The requirement for the macrolens relay was that it should have enough field of view to relay the optical beams out of the PBS+QWP assembly to the next stage with minimum aberration. A telecentric relay system was used for maximum alignment tolerance. Ray-trace simulation showed that the use of a pair of achromatic doublets with a focal length of 30 mm would provide a sufficient field of view to relay the optical beams coming out of the PBS+QWP assembly. Shortening the focal lengths of the relay macrolenses would reduce the overall system size but would require more complex macrolenses. Also, the physical dimensions of the DB's imposed a minimum focal length of $f = 30$ mm for the macrolenses. With the $f = 30$ mm doublets, the separation between stages was 120 mm. However, because of cost considerations $f = 35$ mm doublets were chosen for our system, which resulted in a stage-to-stage separation of 140 mm. Ray-tracing the macrolens relay system by OSLO SIX (OSLO stands for Optics Software for Layout and Optimization³¹) showed that the system had a diffraction-limited performance with a field of view of 2.2 mm (field angle of 1.14°). Since the unidirectional ring contained four DB's with each DB connected to a PCB in the front portion of the VME chassis, the PCB-to-PCB separation was approximately $140/2 = 70$ mm.

The macrolens relay system also contained two sets of adjustment elements, a pair of tilt plates, and Risley beam steerers, as shown in Fig. 4. The pair of tilt plates was used to adjust the lateral positions of the optical beams on the pixelated mirrors of PMMA_{*i+1*}, while the angular directions of the beams impinging on the pixelated mirror were not affected. The Risley beam steerers were used to control the angle of incidence of the optical beams with respect to the pixelated mirrors on PMMA_{*i+1*} so that the reflected beams from the pixelated mirrors could be directed normal to the microlenses on MA_{*i+1*}.

The pair of tilt plates consisted of two 1.5-mm-thick glasses (SF10) mounted at a fixed angle of 10° to the optical axis of the macrolens system. When the tilt plates were rotated with one another, the tilt angle of

the pair could be adjusted continuously; therefore the optical beams could be controlled laterally. This approach was well suited to the optomechanical system design that used barrel housing in a slot-rod base-plate.²⁴ The drawback of this approach was that the movement of the optical beams at the surfaces of the pixelated mirrors was not orthogonal. The maximum adjustable lateral offset of the optical beams on the pixelated mirrors was 219 μm . Ray-trace simulation showed that, when the tilt angle was smaller than 10° , the introduced astigmatism was negligible. The Risley beam steerers consisted of a pair of 2-mm-thick wedges (SF10) with identical wedge angles of 1° . The maximum deviation angle was approximately 1.4° , which corresponded to a lateral displacement of 435 μm at the surface of the pixelated mirrors of PMMA_{*i+1*} and consequently approximately 700 μm at the surface of MA_{*i+1*}.

With the beam-steering capability provided by the pair of tilt plates and Risley beam steerers, the optical beams could be adjusted accurately with respect to the pixelated mirrors of PMMA_{*i+1*} and consequently focused at the detector array by the microlenses of MA_{*i+1*}. More details regarding the adjustment of the pair of tilt plates and the Risley beam steerers for implementing the stage-to-stage optical interconnect are given in Section 6.

B. Image Mapping

Understanding the image mapping between stages is important since it affects the physical layout of the smart-pixel transceivers. A general discussion of image mapping by use of a matrix representation was presented previously in Ref. 26. As in the reference, we choose the coordinate system such that the z axis always points in the same direction as that on which the beams are propagating (therefore the direction changes as the beams are deviated), and the x , y , and z axes form a right-hand Cartesian coordinate system. The y axis is chosen to be parallel to the reflection surface of the beam splitter in the optical relay system. In addition, $W_n[i, j]$ is used to represent the optical aperture of the transceiver (i, j) at stage_{*n*}.

For the stage-to-stage interconnects without the two turning mirrors, the optical beams transmitted from the modulator array to the detector array will encounter three reflections (two reflections from the two PBS reflection surfaces and one reflection from the pixelated mirrors), one telecentric relay system (the macrolens relay), and one transformation of the coordinate system (when the beams start from the modulator array). Therefore image mapping can be expressed as $W_n[i, j] \rightarrow W_{n+1}[N - i + 1, N - j + 1]$.

For the stage-to-stage interconnects involving the two turning mirrors, imaging mapping becomes more complicated. The two turning mirrors introduce additional $+90^\circ$ and -90° rotations with respect to the direction of the optical beam propagation (z axis). The effects of these two coordinate transformations are not canceled. As a result, an additional imaging permutation of $W_n[i, j] \rightarrow W_{n+1}[N - i + 1, N - j +$

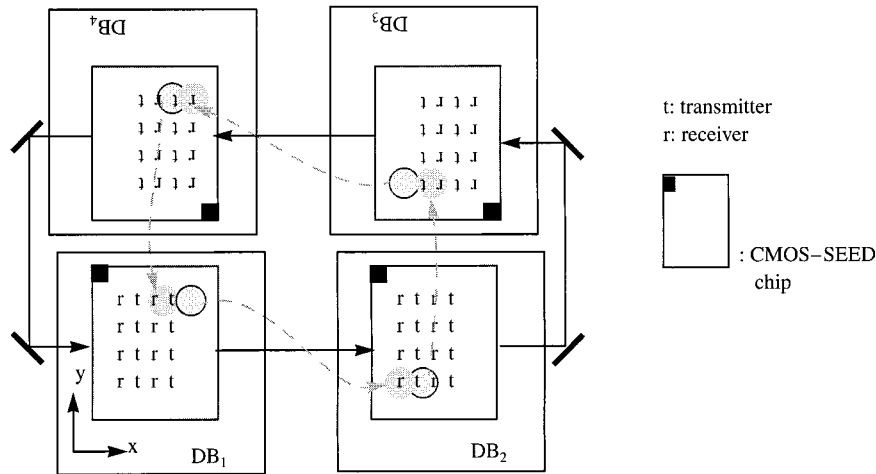


Fig. 7. Schematic of the CMOS-SEED chips on the DB's in the unidirectional ring.

1] is added to the normal imaging mapping. Therefore stage-to-stage imaging mapping can be expressed as $W_n[i, j] \rightarrow W_{n+1}[i, j]$.

If we choose stage₁ as the starting point, the optical beams from the modulator (i, j) at stage₁ will end up on the detector ($N - i + 1, N - i + 1$) at stage₂. The optical beams from the modulator ($N - i + 1, N - i + 1$) will end up at the detector ($N - i + 1, N - i + 1$) on stage₃. These relations can be expressed as

$$\left[\begin{array}{l} W_4[i, j] \leftarrow W_3[N - i + 1, N - j + 1] \\ W_1[i, j] \rightarrow W_2[N - i + 1, N - j + 1] \end{array} \right]. \quad (4)$$

Figure 7 shows the image mapping for the four CMOS-SEED chips on the DB's. An optical signal from a modulator will end up on a detector on the next stage according to expression (4). Such an arrangement ensured that the four CMOS-SEED chips on the four DB's had the same orientation.

C. Alignment Tolerances

The alignment tolerance is an important factor when one is designing and comparing various optical systems. It drives the design of the optomechanical system and sets the machining tolerances of the mechanical components. For this analysis the alignment tolerance of each optical component in a degree of freedom was defined as the maximum allowable offset in that degree of freedom from its nominal position that resulted in a certain percentage power drop (e.g., ~5%) from the maximum power throughput. This percentage is chosen on the basis of the balance among the maximum allowable optical power from the laser source, the minimum optical power required by the receivers, and the achievable machining accuracy of the optomechanics. A large percent drop will allow for large alignment tolerances but will result in a large power loss. The analysis for alignment tolerance of an optical system has been studied

previously for several specified system configurations.^{19,25,32}

For the hybrid optical system used in the back-plane demonstrator, the microlens relay was the part of the interconnect with the most stringent alignment tolerances. This is due mainly to the highly conjugate nature of the maximum lens-to-waist configuration of the microlens relay.³³

This section is organized as follows. The analysis results³³ are briefly summarized and applied to the microlens relay in the hybrid optical system. Then the clipping effect of the Gaussian beams propagating through the finite apertures of the microlenses is discussed. Finally, the alignment tolerance of the overall system is presented.

1. Alignment Tolerances of the Microlens Relay

For a symmetric microlens interconnect that relays optical beams from laser sources to the receiver array, the alignment tolerances have been studied for various offsets of the system parameters.³³ It is assumed that Gaussian beam-propagation theory is valid when the offsets of the optical elements in the microlens interconnect are small. The effects of off-axis Gaussian beam propagation³⁴ have been taken into account in the analysis. It can be shown that the microlens relay with a maximum lens-to-waist configuration is sensitive to the misalignment of the laser source when the ratio of the z_r/f is small, where z_r is the Rayleigh range of the Gaussian beam and f is the focal length of the microlenses. Refer to Fig. 6: If the laser source is laterally offset δ_0 from the optical axis, the lateral displacement of the Gaussian beam at the second microlens would be

$$\delta_2 = (1 + f/z_r)\delta_0. \quad (5)$$

For the microlens relay the beams at a PAP have the least tolerance for misalignment since the offsets are magnified throughout the microlens relay system. As a result, the power throughput is sensitive to misalignments of the beams at the PAP. However, it should be noted that an offset of the optoelec-

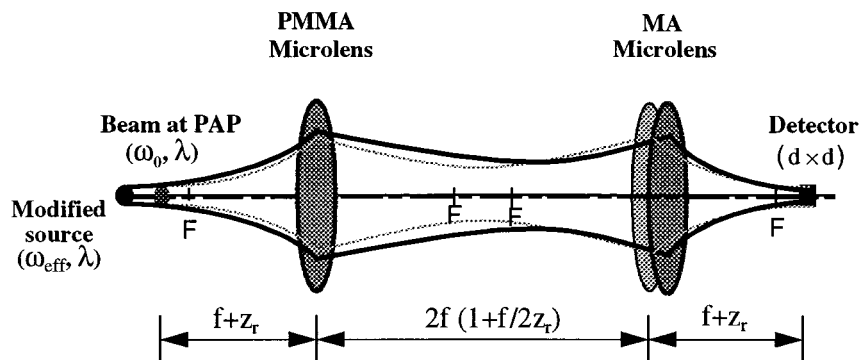


Fig. 8. Clipping effects for the symmetry of the alignment tolerance. To maintain the symmetric distribution of the alignment tolerance, it was necessary to pull the PAP away from the microlens on the PMMA, and the separation between the microlenses was increased.

tronic chip in the hybrid optical system can be considered as a source offset for the microlens relay at the next stage. Similar arguments should apply to the pixelated mirrors on the PMMA where the signal beams from the previous stage were reflected. Therefore the overall optical power throughput is sensitive to the misalignment of the transceiver array and the PMMA.

2. Weak Clipping Effects

When a Gaussian beam propagates through an aperture of finite dimension, the beam is clipped. If the clipping is weak, the clipped beam can be approximated as another unclipped Gaussian beam with an effective beam waist of ω_{0eff} ^{19,28}:

$$\omega_{\text{0eff}} = \omega_0 \left[1 - \exp(-k^2) \cos\left(k^2 \frac{z}{z_r}\right) \right], \quad (6)$$

where z is the distance between the beam waist ω_0 and the aperture, $k = a/2\omega_L$ is the clipping ratio, ω_L is the beam radius on the aperture, and a is the diameter of the circular aperture. In our analysis we assume that this approximation is still valid for a square aperture of dimensions $a \times a$. Therefore the alignment tolerance can still be obtained.

However, after the diffractive effects resulting from the weak clipping of the Gaussian beam propagation are taken into account, the longitudinal alignment tolerances for the microlens relay system would not be symmetric around their nominal positions (for example, an element may have a longitudinal alignment tolerance of $+10 \mu\text{m}/-50 \mu\text{m}$). Such asymmetric distributions of the alignment tolerances tend to increase the difficulty of specifying tolerances for the optomechanical system. For obtaining the symmetric distribution of the alignment tolerance while the optical beam waists on the MA and the PMMA microlenses are kept the same, the location of the PAP must be pulled away from the PMMA microlens and the separation between the PMMA and the MA must be increased, as illustrated in Fig. 8.

3. Alignment Tolerance of an Overall Optical Interconnect

Analysis of the alignment tolerance for the hybrid relay optical system was carried out in the same way as for the microlens relay system. A MATLAB program was written to calculate the decrease in optical power throughput from the PAP to the modulator array and then to the detector array at the next stage when each optical element was misaligned, one at a time. The weak clipping effects of the Gaussian beam as it passed through each microlens were also taken into account. The reflected beams from the apertures of the modulator array were assumed still to be Gaussian. Clipping effects were neglected for the beams passing through the large macrolenses. For simplicity, the effect of the combined misalignments was not included, i.e., when an optical element was misaligned in one degree of freedom, all other elements were in their nominal positions. It was also assumed that the misalignments of different degrees of freedom were uncorrelated. Therefore the total power loss caused by the misalignments is the sum of the power losses introduced by all elements. Although not exactly true in practice, such a calculation would provide an estimate of the power loss that is due to the misalignment.

Table 1 shows the alignment tolerance for the hybrid optical relay system. The calculation was based on a 5% power drop for some sensitive elements (i.e., the optical spot size, the lateral offset of the optical beams at the PAP, and the lateral offset of the transceiver array) and a 2% power drop for all other elements. A 2% power drop for those sensitive elements would result in alignment tolerances that could not be achieved optomechanically. If the machining and assembling tolerances are kept below the set of tolerances listed in Table 1, an estimate of the worst-case misalignment losses can be calculated. With the above assumptions, the optical power loss that is due to worst-case misalignment was estimated to be 29.3% for the optical beams from a PAP to the corresponding modulator array and 40.4% for the optical beams from the PAP to the detector array at the next stage. In addition, the optical power loss that

Table 1. Alignment Tolerances of Stage-to-Stage Optical Interconnects

Optical Components	Offsets	Nominal Values	Alignment Tolerance
Optical beams at the PAP	Optical spot size	6.47 μm	$\pm 0.25 \mu\text{m}$
	Separation to PMMA	922 μm	$\pm 20 \mu\text{m}$
	Lateral offset	—	$\pm 4 \mu\text{m}$
	Tilt misalignment	—	$\pm 0.5^\circ$
	Rotational misalignment	—	$\pm 0.2^\circ$
PMMA (500 \pm 30)- μm substrate of fused silica	Focal lengths of microlenses	768 μm	—
	Separation to PBS+QWP assembly	164 μm	$\pm 150 \mu\text{m}$
	Eight-phase-level diffractive lenses	—	$\pm 20 \mu\text{m}$
	123- μm -width pixelated mirrors	—	$\pm 0.2^\circ$
PBS+QWP assembly	Lateral offset	—	$\pm 100 \mu\text{m}$
	5.0-mm PBS cube	—	$\pm 100 \mu\text{m}$
	Zero-order QWP's with 0.82-mm cover	—	$\pm 0.5^\circ$
	Corning 7059 glass	164 μm	$\pm 150 \mu\text{m}$
MA (500 \pm 30)- μm substrate of fused silica	Focal lengths of microlenses	766 μm	—
	Separation to transceiver plane	866 μm	$\pm 15 \mu\text{m}$
	Eight-phase-level diffractive lenses	—	$\pm 15 \mu\text{m}$
		—	$\pm 0.5^\circ$
Transceiver array CMOS-SEED devices	Lateral offset	—	$\pm 1.5 \mu\text{m}$
	Tilt misalignment	—	$\pm 0.5^\circ$
Macrolenses Achromatic doublets	Focal lengths	35 mm	—
	Focal-length mismatch	—	$< 1\%$
	Positions to PBS+QWP assemblies		
	Macrolens 1	30.78 mm	$\pm 300 \mu\text{m}$
	Macrolens 2	24.79 mm	$\pm 300 \mu\text{m}$
	Separation between lenses	66.00 mm	$\pm 500 \mu\text{m}$
	Lateral offset	—	$\pm 100 \mu\text{m}$
Tilt misalignment	—	$\pm 1^\circ$	

is due to clipping by the finite dimensions of the microlenses and the pixelated mirrors was estimated to be 1.3% for the optical beams from the PAP to the modulator array plane and 3.0% to the detector array plane.

D. Power Budget

The power budget of the optical relay system is given in the Table 2. The theoretical power loss (in the second column of Table 2) includes the theoretical efficiency of each optical component, the overall calculated misalignment and polarization losses, and the diffraction loss resulting from the finite dimension of the optical components. For the PMMA and the MA microlenses a theoretical optical efficiency of 94.5% corresponding to an eight-phase diffractive lens was used.³⁵ As the AR coating was deposited on only the nonetched side of the substrate, the total power efficiency of the MA was estimated to be 91.2%. The reflectivity of the pixelated mirrors was estimated to be 96.8%. This value also took into account the two reflections for the optical beams entering into and leaving the fused-silica substrate of the PMMA.

In addition, the polarization loss was also estimated. The variation of retardance of the QWP's ($\pm \lambda/350$), the variation of the incident wavelength ($\pm 1 \text{ nm}$), the position accuracy of the QWP's in the optical system ($\pm 1^\circ$), and the polarization extinction

ratio of the input fiber (the ratio of $|v_y|^2$ to $|v_x|^2$ between 80:1 and 100:1) were taken into account. The maximum polarization power losses between the fiber input and the modulator plane were approximately 2%, and the maximum polarization power losses from the fiber input to the detector plane were approximately 8%.

To measure the optical power budget experimentally without being concerned with the performance of the CMOS-SEED devices, we introduced a custom amplitude mask at the modulator array plane instead of a CMOS-SEED chip. This amplitude mask consisted of an array of reflective mirrors (chromium films) that had the same pattern and dimensions (20 $\mu\text{m} \times 20 \mu\text{m}$) as the apertures of the modulator array. The reflectivity of the chromium mirrors was estimated to be 65.0%.

The analysis shows that the power throughput from the fiber input to the corresponding transmitter array plane had an upper bound of -18.7 dB (1.35%) (when all the optical elements were in their nominal positions) and a lower bound of -20.2 dB (0.95%) (when all the optical elements were misaligned by an amount equal to their calculated alignment tolerance). The power through from the fiber input to the detector array plane at the next stage had an upper bound of -22.3 dB (0.6%) and a lower bound of -24.5 dB (0.35%). These values included the power-

Table 2. Optical Power Budget for Stage-to-Stage Interconnect

Components	Estimated Component Throughput ^a (%)	Measured Component Throughput (%)
Fiber input at stage _{<i>i</i>}	100	100
All beams at PAP _{<i>i</i>}	73.0	68
One beam at PAP _{<i>i</i>} (due to fan-out loss)	1.83	1.7
Microlens at PMMA _{<i>i</i>}	91.2	89
PBS + QWP (<i>T</i>) at stage _{<i>i</i>}	95.5	95
Microlens at MA _{<i>i</i>}	87.5	89
Diffraction effect up to transmitter plane (clipping loss, 1.3%)	98.7	
Polarization effect up to transmitter plane (worst-case polarization loss, 2.0%)	98.0	
Misalignment effect (worst-case power loss, 29.3%)	70.7	
Subtotal power TP (worst case) at transmitter plane at stage _{<i>i</i>}		
Upper bound	1.35 (−18.7 dB)	1.2 (−19.1 dB)
Lower bound	0.95 (−20.2 dB)	0.9 (−20.6 dB)
Amplitude mask ^b	65.0	65
MA _{<i>i</i>}	91.2	89
PBS + QWP (<i>R</i>) at stage _{<i>i</i>}	98.5	96
Tilt plate pair	99.0 ²	98.6 ² = 97
First macrolens	99.6	97
Turning mirrors	99.0 ²	(98)
Second macrolens	99.6	97
Risley beam steers	99.0 ²	98.6 ² = 97
PBS + QWP (<i>R</i>) at stage _{<i>i+1</i>}	98.5	95
Mirror at PMMA _{<i>i+1</i>}	97.8	98
PBS + QWP (<i>T</i>) at stage _{<i>i+1</i>}	95.5	95
Microlens at PMMA _{<i>i+1</i>}	91.2	89
Diffraction effect from transmitter plane to Rx plane (clipping loss, 1.3%)	98.7	
Polarization effect from transmitter plane to Rx plane (worst-case polarization loss, 6.1%)	93.9	
Misalignment effect from transmitter plane to receiver plane (worst-case power loss, 15.7%)	84.3	
Total power TP at receiver plane at stage _{<i>i+1</i>}		
Upper bound	0.59 (−22.3 dB)	0.41 (−23.8 dB)
Lower bound	0.35 (−24.5 dB)	0.25 (−26.1 dB)

^aThe estimated component throughput was obtained from component specifications or theoretical calculations when required.

^bIf the amplitude mask were replaced by the CMOS-SEED chip with the reflectivities of the modulator array to be 30% for the transmission state and 15% for the absorption state, the theoretical upper bounds and lower bounds of the optical power throughput at the detector array plane would be as follows: The upper bound would be 0.19% (−27.2 dB) for the transmission state and 0.10% (−30.2 dB) for the absorption state; the lower bound would be 0.12% (−29.4 dB) for the transmission state and 0.06% (−32.4 dB) for the absorption state.

splitting loss caused by the fan-out grating in the OPS.

The estimated power budget based on the measured efficiencies of the components used in the hybrid optical system is shown in the third column of Table 2. Based on the measured power efficiencies of the optical components, the overall power throughput was estimated as follows: For the optical beams from the fiber input to the modulator array plane, the upper bound was −19.1 dB (1.23%) and the lower bound was −20.6 dB (0.87%); for the optical beams to the detector array plane, the upper bound was −23.8 dB (0.41%) and the lower bound was −26.1 dB (0.25%).

If the amplitude mask were replaced with the CMOS-SEED chip with the reflectivity of the modulator array to be 30% for the transmission state and 15% for the absorption state, the upper bound and the

lower bound of the optical power throughput from the fiber input to the detector array would be calculated to be −27.2 dB (0.19%) and −29.4 dB (0.12%), respectively, for the transmission stage and −30.2 dB (0.10%) and −32.4 dB (0.06%), respectively, for the absorption state. These values are used as the reference values in the experimental comparison.

4. Optical Component Characterization

A. Microlens Array

The focal length and the power efficiency of several microlenses were measured. The focal length of a microlens was obtained by the measurement of the distance between the surface of the microlens and the position of the focal plane. The inaccuracy of the measurement was due to the uncertainty in defining the focal plane, since the depth of the focus was rel-

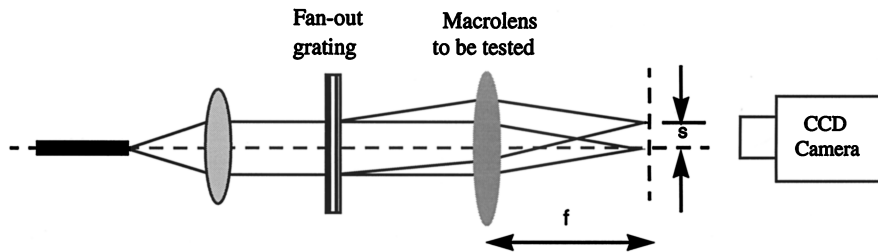


Fig. 9. Setup used for measuring the relative focal length of a macrolens.

atively large. The measured focal length was $f = 765 \pm 10 \mu\text{m}$ at a wavelength of 850 nm.

To measure the power efficiency of a microlens, we focused a collimated optical beam by using a slow lens ($\sim f/10$) at the front focal position of the microlens. Since the f -number of the microlens was smaller than that of the focusing lens, more than 99.9% of the optical power was collected by the microlens. The optical beam was then recollimated after the microlens. Therefore, when the incident optical power and the exit optical power are measured, the efficiency of the microlens can be obtained. This efficiency corresponded to the diffraction efficiency of the optical power into the first-order diffracted beam. The measured power efficiency of a microlens was 92% (with the reflection loss at the surface of the substrate taken into account, the power efficiency of a microlens was adjusted to 89%). This value is close to the theoretical efficiency of 94.5%.

Some microlenses had particles of dust on their surfaces. These particles scattered the incident light and reduced the diffraction efficiency. As a result, the optical power throughput in these particular channels was reduced and the optical cross talk between microlens channels increased. Consequently, the power uniformity of the optical beams onto the modulator array and the detector array at the next stage was reduced.

B. Polarizing Beam Splitter and Quarter-Wave Plate Assembly

The PBS was specified with a 96.2% transmission for p -polarized light and less than 0.07% transmission for s -polarized light at a wavelength of 850 nm. The transmission efficiency of the PBS+QWP assembly for a circularly polarized beam was measured to be better than 95%. The transmission wave-front distortion was found to be better than $\lambda/2$ at 633 nm across 80% of the aperture. Beam deviation for the transmitted light was less than 5.0 arc min.

C. Macrolens

It is required from the alignment tolerance simulation that the focal lengths of a pair of macrolenses in a macrolens relay be matched to within $\pm 0.5\%$. However, most commercial vendors usually specify the focal lengths to within only $\pm 1\%$ accuracy. Because we were concerned with only the relative focal lengths of the macrolenses instead of the absolute values, we used a fan-out grating, as shown in Fig. 9,

to measure the relative focal lengths of the macrolenses.

Assuming that the periodicity of the fan-out grating is P , then the spot separation on the focal plane will be $s = \lambda f/P$, where λ is the wavelength of the optical beam and f is the focal length of the macrolens to be tested. Therefore, by measuring the spot separation, we can obtain the relative focal lengths of the macrolens (gauged by the periodicity of the fan-out grating). The mismatching of the focal lengths for two macrolenses with measured spot separations of s_1 and s_2 can be found from

$$\left| \frac{\delta f}{f} \right| = \left| \frac{f_1 - f_2}{f_1} \right| = \left| 1 - \frac{s_2}{s_1} \right|. \quad (7)$$

The measured spot separation was approximately $345 \mu\text{m}$. The measurement error for the spot separation was less than $1.5 \mu\text{m}$. Therefore the error for focal-length measurement was less than $\pm 0.42\%$, which was within the design requirement. This approach allowed us to select four pairs from 10 macrolenses, with each pair having a focal-length mismatch within $\pm 0.5\%$.

5. Prealignment of the Optical System

A. Polarizing Beam Splitter and Quarter-Wave Plate

For mounting a PBS+QWP assembly, a collimated optical beam from a diode laser ($\lambda = 760 \text{ nm}$) was apertured into a vertical line shape and was directed onto the PBS+QWP assembly. The PBS+QWP assembly was adjusted such that the reflected optical beam was normal to the component and, at the same time, the orientation of the line was also vertical. The reflected beam was used since it was twice as sensitive to the angular misalignment of the PBS+QWP assembly. These two conditions ensured that the PBS+QWP assembly was mounted with minimum rotational or tilt misalignments. The PBS+QWP assembly was then glued onto a mechanical mount. The aligned PBS+QWP assembly was less than 0.05° away from the normal reflection angle, and the orientation of the line shape was less than 0.1° away from the vertical direction.

B. Microlens Array to Pixelated Mirrors–Microlens Array

The MA and the PMMA were glued onto opposite sides of the mechanical mount of the PBS+QWP assembly. The MA-to-PMMA prealignment involved

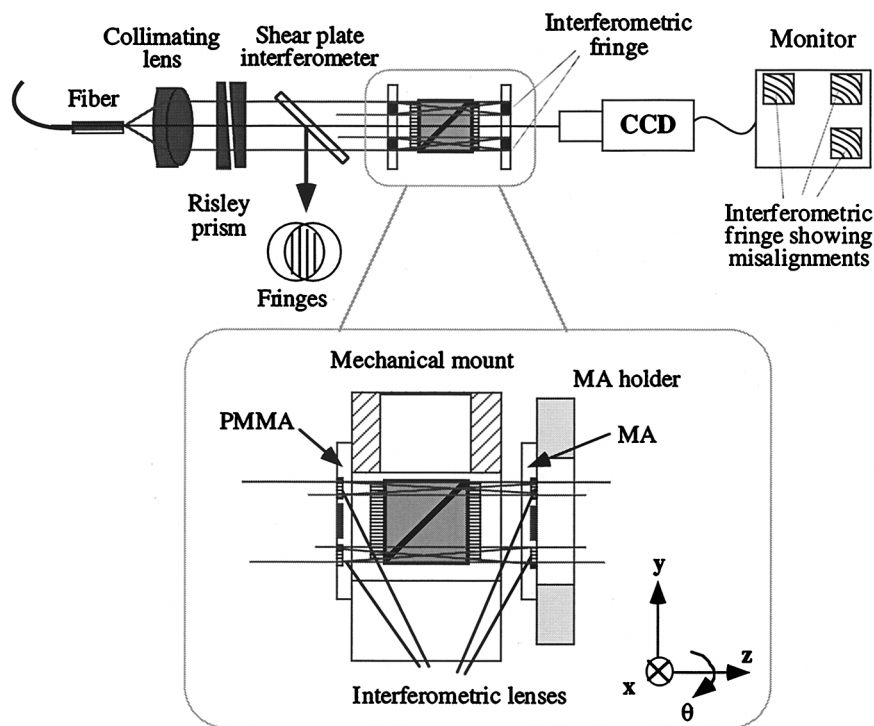


Fig. 10. Setup for the PMMA-to-MA alignment.

two steps. In the first step the PMMA was glued onto its mechanical mount. The PMMA and the MA substrates were designed with alignment markers (chromium lines) that matched two mechanical references on the mount. The PMMA was coarsely positioned to within $\pm 100 \mu\text{m}$ with respect to the mechanical axis of the mount. It was noted that the lateral position error of the PMMA was not critical since we could correct this error by adjusting the position of the optical beams at the PAP by using the Risley beam steerers in the OPS. However, the rotational error of the PMMA to the PBS+QWP assembly in the mount was critical since there was no built-in mechanism in the optical relay system to correct for this misalignment error. The effect of this rotational error is discussed further in Subsection 6.B.

The second step of the prealignment involved aligning the MA to the PMMA. The alignment between these two elements was carried out with an interferometric alignment technique.³⁰ The basic principle behind the interferometric technique involves the use of two diffractive microlenses to generate an interference pattern. The focal length of the interferometric lens was designed to be exactly half the distance between the PMMA and the MA. A normal incidence, coherent optical beam was diffracted by the interferometric lens on the PMMA. The interferometric lens was designed such that most of the optical power was evenly divided into the zero-order (nondiffracted) beam and the first-order diffracted beam. The first-order diffractive beam was recollimated by the corresponding interferometric lens on the MA and interfered with the zero-order

beam. The MA-to-PMMA prealignment was achieved when the desired fringe pattern was obtained.

The alignment setup is shown in Fig. 10. A He-Ne laser beam output from a single-mode fiber was collimated by an achromatic doublet. The collimation was monitored by use of a commercial shear plate interferometer. Risley beam steerers were adjusted to ensure that the He-Ne beam was incident normal to the surface of the PMMA. When the MA was brought into position, a series of interferometric fringes was formed. The fringes were imaged onto a CCD camera for further processing and analysis. Figure 11 shows the interference fringes observed as the MA was brought into alignment with the PMMA. Figure 11(a) illustrates the fringe pattern for the case in which the two MA's were rotationally misaligned in θ and misaligned in the x , y , and z directions. When the second MA was moved closer to its nominal position, the number of fringes observed was reduced. Figure 11(b) shows the fringe pattern for the situation in which the rotational misalignment was corrected and misalignment in the y direction was dominant. Final alignment was obtained when the number of fringes was minimized as shown in Fig. 11(c). The MA was glued onto the mechanical mount and the MA holder was detached.

The dimensions of the mechanical mount were slightly larger than those specified; this was mainly due to the anodization step that followed the machining of the mount. In addition, the finite thickness of the glue used to attach the MA and the PMMA to the mount was of the order of 0.10–0.15 mm. Using the standard traveling microscope technique, we verified

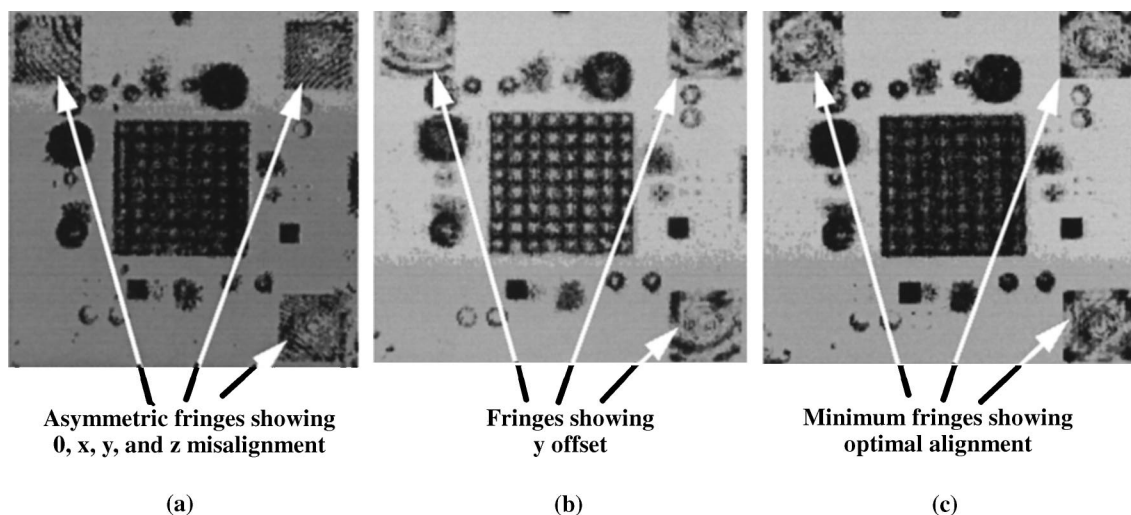


Fig. 11. Fringe pattern providing information on the alignment of the MA to the PMMA, where (a) asymmetric fringes show the θ and z misalignments, (b) one-sided fringes show the lateral misalignment, and (c) minimum fringes indicate the optimal alignment.

the OPL between the PMMA and the MA to be 5.60 ± 0.01 mm. From the final fringe patterns observed we estimated that the longitudinal offset was less than $150 \mu\text{m}$, the lateral offset was less than $4 \mu\text{m}$, and the tilt and rotational offsets were less than 0.1° . These misalignment errors all fall within the specified tolerances, as shown in Table 1. For simplicity, a mounted PBS+QWP assembly with the aligned PMMA and MA is hereafter referred to as a microlens relay module (MR module).

6. Optical System Assembly

The first step in system assembly was to align the four turning mirrors on the baseplate. These mirrors defined the optical axis of the unidirectional ring. Next the four MR modules were inserted and aligned to the optical axis of the ring. Afterward, the OPS was aligned to the corresponding MR module. The macrolens system, the tilt plates, and the Risley beam steerers were then adjusted. Finally, the DB's with CMOS-SEED chips were mounted and clamped into their correct positions. This section describes the step-by-step alignment procedure developed for the optical system assembly.

A. Alignment of the Turning Mirrors

The four turning mirrors, as shown in Fig. 2, were used to close the loop of the unidirectional ring interconnect. Any errors in tilt and rotational misalignments of the mirrors would not only cause a change in the OPL but would also introduce an image rotation of the 2-D array of beams from stage₂ to stage₃ and from stage₄ to stage₁. However, a controlled amount of this image rotation can be introduced by tilt and rotation of the turning mirrors to compensate for the image rotation of the 2-D array of beams caused by other misalignments in the system.

It should also be noted that adjusting the turning mirrors to correct the rotational error would also

cause a shift of the 2-D array of optical beams from the nominal position of the detector arrays. This unwanted displacement can be corrected only by adjustment of the tilt-plate pair and the Risley beam steerers, which have a limited range of adjustments, as described in Subsection 3.A. Therefore it was required that the mirrors be aligned as close as possible to their optimal positions.

A He-Ne laser beam was launched through a pellicle and adjusted to travel along the optical axis of the ring. The optical axis of the unidirectional ring was defined by the center of a series of alignment apertures that were placed along the slot of the baseplate. For convenience, we refer to this axis as the optical axis of the ring. The turning mirrors were adjusted one by one such that the reflected beam was always traveling along the optical axis of the ring.²⁴

B. Alignment of the Microlens Relay Module to the Optical Axis of the Ring

For accurately aligning the MR module with the optical axis of the ring, a collimated He-Ne beam was sent along the optical axis from the PMMA side of the PBS+QWP assembly. The MR module was adjusted such that the reflected beam from the PBS+QWP assembly was directed along the optical axis of the ring.

However, because the PBS+QWP assembly had approximately a 5-arc min deviation angle and the rotational error had occurred during MA-to-PMMA prealignment (as mentioned in Subsection 5.B), the reflected beam could not be aligned perfectly to the optical axis of the ring. This beam deviation would cause a rotational error of the 2-D array of optical beams from the modulator surface to the detector array. Correction of the image rotation was necessary to complete the loop of the unidirectional ring. The technique for correcting this rotational error is presented in Subsection 7.A.

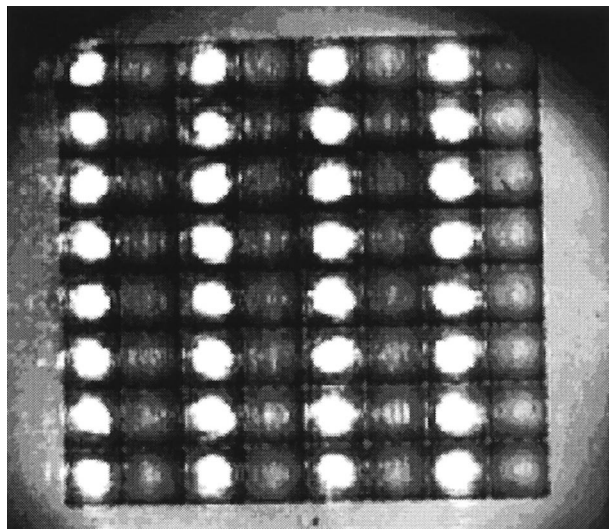


Fig. 12. Optical beams from stage_{*i*} on the microlenses of MA_{*i*}.

C. Optical Power Supply to Microlens Relay Module Alignment

The alignment required that (1) the OPS be 922 μm away from the PMMA of the MR module so that the focused beams would be located 866 μm away from the MA, as specified in Table 1; (2) the optical beams be centered and travel normal to the PMMA and the MA microlenses; and (3) the optical beams have maximum transmission. This was achieved by trial-and-error adjustment of the Risley prism at the OPS, the position of the OPS, and the rotation of the QWP in the OPS.

It was found that the optical beams on the MA were sensitive to the rotation of the spot array at the PAP. It can be derived from Eq. (5) that a small rotational error of θ for the optical beams at the PAP would result in a relatively large rotational error of $(1 + f/z_r)\theta$ for the optical beams on the MA. The rotational error would have a significant effect on a large array of beams with large pitch. For a 4×8 array of beams with a 125-μm pitch in the microlens relay, a 0.1° rotational error for the spot array at the PAP would result in an approximately 0.7° rotational error of the beams on the MA, which corresponds to a lateral offset of 8.8 μm on the MA. This large offset of the edge optical beams on the microlenses of the MA would affect the optical power throughput of the beams; consequently, nonuniformity of the optical power to the transceiver array would increase. Thus the adjustable resolution of the Risley beam steerers in the OPS should be better than 0.1°.

Figure 12 shows a frame grab of the optical beams at the MA microlenses. The alignment showed that the optical beams were within ± 5 μm of the centers of the microlenses with a rotational error of less than 0.05°. The results also confirmed that the MA-to-PMMA prealignment was accurate.

D. Macrolens Relay Alignment

The macrolens relay had to be aligned so that the beams from stage_{*i*} would impinge on the centers of

the pixelated mirrors of PMMA_{*i+1*} and then be reflected on the microlenses of MA_{*i+1*}. The reflected beams from the pixelated mirrors should be normal to the microlenses on MA_{*i+1*} so that the focused beams after MA_{*i+1*} are incident upon the apertures of the detector array at stage_{*i+1*}. The divergence of the beams also had to be corrected so that the focused spots appeared 866 μm away from the surface of MA_{*i+1*}. Therefore the optical beams from the OPS at stage_{*i+1*} and the relayed optical beams from stage_{*i*} were focused on the same plane, the device plane of stage_{*i+1*}.

The reflected optical beams from the modulator array plane were used to align the microlenses. For this purpose, a custom amplitude mask (described in Subsection 3.D) was used. The amplitude mask was placed 866 μm away from the surface of the MA substrate. The position of the amplitude mask was monitored by a CCD camera on a motorized *x-y-z* translational stage. Since the amplitude mask was partially transparent, it was possible to define the position of the mask accurately. The use of the amplitude mask not only simplified the alignment procedure but also provided us with a way to characterize the performance of the optical system without being concerned with the nonideal performance of the optoelectronic devices.

The first step was to adjust the location of the macrolenses until the focused spots were obtained 866 ± 16 μm away from the surface of MA_{*i+1*}. Next, the optical beams were aligned with respect to the pixelated mirrors of PMMA_{*i+1*} and the microlenses of MA_{*i+1*} simultaneously. This alignment was achieved by adjustment of the pair of tilt plates and the Risley beam steerers.

As was mentioned in Subsection 5.B, rotational misalignment was a concern. The method used for correcting the image rotations depended on whether the stage-to-stage relay included the turning mirrors. For a stage-to-stage interconnect that did not include turning mirrors (stage₁ to stage₂ and stage₃ to stage₄), this correction was carried out by a slight rotation of OB₂ with respect to OB₁ and OB₃ with respect to OB₄. It turned out that this method was satisfactory if the initial image rotation was small. For the stage-to-stage interconnect that included turning mirrors (stage₂ to stage₃ and stage₄ to stage₁), the image rotation was corrected by adjustment of both turning mirrors in the relay. These correction methods caused a displacement of the optical beams on the microlenses of MA_{*i+1*}, which could be compensated for by adjustment of the pair of tilt plates and the Risley beam steerers. As was pointed out in Subsection 6.A, the limited range of adjustment of these elements meant that only a small image-rotation error could be corrected. In both cases of adjustment, the original rotation error of approximately 0.2° was corrected.

Figure 13 shows the optical beams from stage_{*i*} and stage_{*i+1*} incident upon the microlenses of MA_{*i+1*}. The alignment reveals that the optical beams from stage_{*i*} were within ± 5 μm of the centers of the mi-

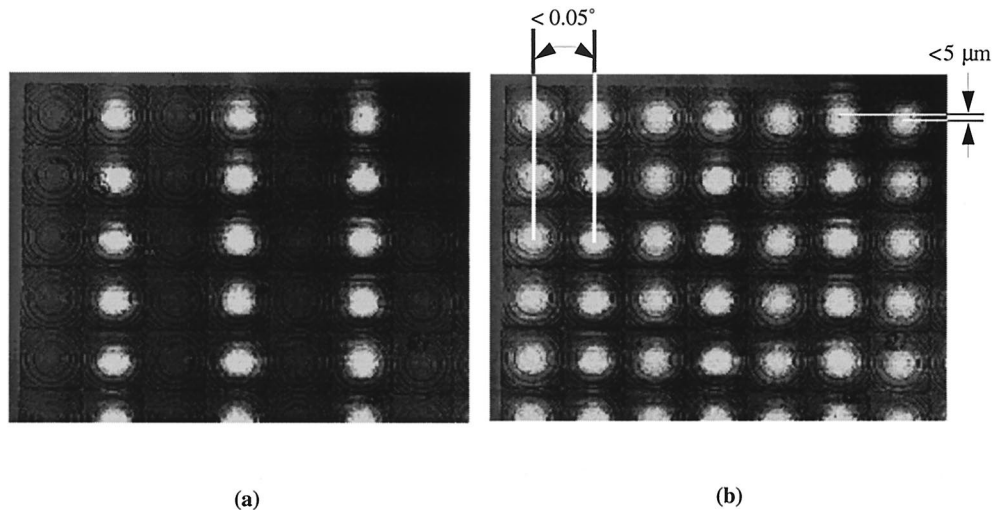


Fig. 13. Optical beams from stage_{*i*} and stage_{*i*+1} incident on the microlenses at MA_{*i*+1}: (a) Optical beams from PAP_{*i*} incident on MA_{*i*+1}. (b) Optical beams from both PAP_{*i*} and PAP_{*i*+1} incident on MA_{*i*+1}.

colenses of MA_{*i*+1}. The rotational error was less than 0.05°.

E. Optoelectronic Device to Optical System Alignment

After the microlens relay and the macrolens relay were aligned, the DB's with surface-mounted CMOS-SEED optoelectronic chips were aligned. We obtained coarse alignment by luminescing the CMOS-SEED and monitoring with an imaging system. The final position was obtained when the modulated light was maximum on the receiver array at the next stage. As the microlens relay and the macrolens relay had been prealigned with the aid of the amplitude mask, the alignment of the optoelectronic device to the optical systems turned out to be successful.

7. Optical System Characterization

This section describes the performance of the optical system. For testing the optical performance of the hybrid interconnect system, the optical power throughput, the spot uniformity, the spot sizes, and the positions of the focused spots at various accessible locations of the optical system were compared. These locations included the modulator array and the detector array planes (866 μm away from the surface of the MA's), as well as the PAP at the output of the OPS. The characteristics of the optical beams at the PAP were determined in a separate test rig since it was impossible to measure the optical beams at the PAP in the backplane system because of the spatial constraints. To measure the optical performance at the detector array plane, we used an amplitude mask, as described in Subsection 7.D.

Because it is difficult to measure the optical power of a single beam within the 4 × 8 array of beams pitched at 125 μm, a 10× microscope objective was used to increase the separation of the beams and a 500-μm-diameter pinhole was used to allow only the desired beam to pass through. To eliminate the ef-

fect of source power fluctuations, we used a dual-channel optical power meter to measure the relative power of each optical beam with respect to a reference optical power. The throughput of the microscope objective was calibrated beforehand with a single beam of known input and output.

To measure the power uniformity across an array, we moved the microscope objective and the pinhole laterally, measuring the optical power of each spot in the array one by one. However, this method was time consuming. Alternatively, the power uniformity of the spot arrays could also be obtained with a high-resolution linear CCD camera and a microscope objective. The image of a spot array was digitized (frame grabbed), and the relative optical power per spot was obtained by integration of the pixel values associated with each optical spot. The results obtained with this method were very close to those obtained with the pinhole technique as long as the background noise was subtracted. The measurement difference was less than 0.5%. This digitizing method provided a fast way to perform the uniformity measurement. It also reduced the measurement error that was due to mode variation in the optical source, which caused a small fluctuation of the optical powers between the spots in the array and consequently a small variation of array uniformity with time. However, for a large array of beams a microscope objective with small magnification had to be used to capture the whole array of spots. As a result, each spot contained only a few pixels. Therefore the measurement accuracy was reduced. In the system characterization, we used both methods to perform the power uniformity measurement.

The spot separation and the spot size of a spot array were also measured with a high-resolution linear CCD camera and a microscope objective. We obtained the spot separation by counting the pixel numbers between the spots. To increase the measurement accuracy, we used a microscope objective

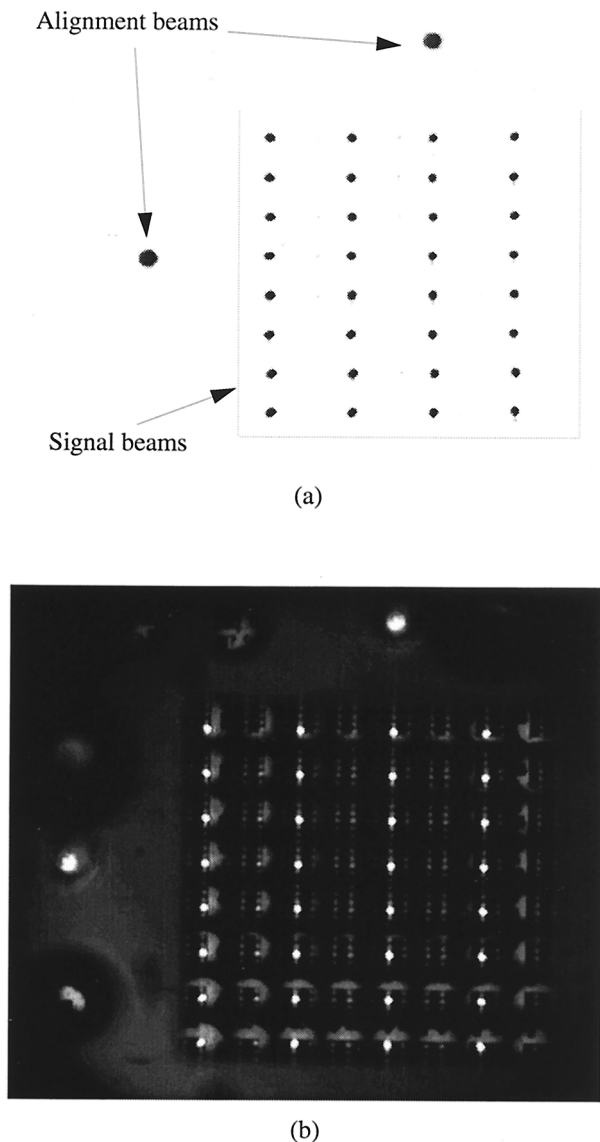


Fig. 14. Spot arrays at the modulator plane of stage₃: (a) Spot array. (b) Spot array with illumination light. The background shows the multiple images of the PMMA imaged by the MA.

with high magnification to increase the number of the pixels between the spots. The pixel scale was calibrated with a high-resolution Ronchi ruling. The center position of each spot was obtained from the centroid of the pixels belonging to each spot. For measuring the spot size of each optical beam, a Gaussian beam profile was curve fitted to the spot profile obtained from a digitized image of the spot. The convolution effect of the microscope and the CCD camera was corrected with the method described in Ref. 36. The optical beam radius at $1/e^2$ was used as the approximate spot size. We confirmed the precision of this measurement method by comparing it with the results obtained with a precision scanning-slit beam profiler. We assessed the optical performance of the interconnect by measuring the spot sizes, the spot positions, the power uniformity, and the power throughput for the optical interconnect

from stage₁ to stage₂ (which had no turning mirror) and from stage₂ to stage₃ (which included two turning mirrors).

A. Spot Sizes and Spot Positions

The spot sizes of the optical beams at PAP₁ and PAP₂ were measured to be $6.8 \pm 0.2 \mu\text{m}$. Figure 3 shows the spot array generated at PAP₁. Variation of the spot size was measured to be less than 1.0%. The spot size at the edge of the array was approximately $0.1 \mu\text{m}$ larger. The vertical pitches between spots were measured to be $125.2 \pm 0.1 \mu\text{m}$ and $125.7 \pm 0.1 \mu\text{m}$ for the spot arrays at PAP₁ and PAP₂, respectively.

As was stated in Subsection 6.C, the focused optical beams at each stage were within $866 \pm 16 \mu\text{m}$ from the surface of the MA's. However, the average spot sizes at the modulator array planes of stage₁ and stage₂ were reduced to $6.0 \pm 0.3 \mu\text{m}$ and $5.8 \pm 0.3 \mu\text{m}$, respectively. This decrease in the spot size at the modulator planes was mainly due to the increase in the spot sizes at the PAP of stage₁ and the PAP of stage₂. It should be noted that the increase in the spot sizes at the PAP's increased the optical power loss as a result of more clipping losses of the optical beams at the MA microlenses. This also means an increase in the optical cross talk between the optical channels. Figure 14 shows the optical spots at the modulator array plane of stage₃.

The variation of the spot sizes at the modulator planes was approximately 2.7%. The spots located on the edge of the array were approximately $0.15 \mu\text{m}$ larger than the spots in the centers of the arrays. This slight increase in the size of the peripheral spots is mainly due to the combined rotational misalignment of the optical beams at the PAP's and the MA-to-PMMA prealignment. The spot pitches were measured to be $125.8 \pm 0.1 \mu\text{m}$ and $126.2 \pm 0.1 \mu\text{m}$, respectively, which corresponds to an 0.08% increase of the spot separation from the PAP's to the modulator arrays.

For the spot array at the detector planes, the measured average spot sizes were $6.7 \pm 0.3 \mu\text{m}$. There was no significant difference in spot sizes between the stage₁-to-stage₂ interconnect and the stage₃-to-stage₄ interconnect. This may be because the reflected signal beams from the apertures of the modulator arrays were aberrated Gaussian beams with beam waists altered by the limited dimensions of the modulators. Some spots were considerably larger than others; this was due to dust contamination of the microlenses. If these spots were discarded, the variation of the spot sizes was approximately 4.4% on the detector planes. The edge spots were not only $\sim 0.3 \mu\text{m}$ larger but also showed astigmatism. The measured spot pitch was approximately $126.3 \pm 0.5 \mu\text{m}$, which corresponds to an $\sim 0.4\%$ increase in the spot separation from the modulator arrays to the detector arrays.

The positions of the optical beams at the device plane of stage_i were compared with the beams relayed from stage_i and the beams from the OPS of stage_{i+1}. Both arrays of beams were focused $866 \pm$

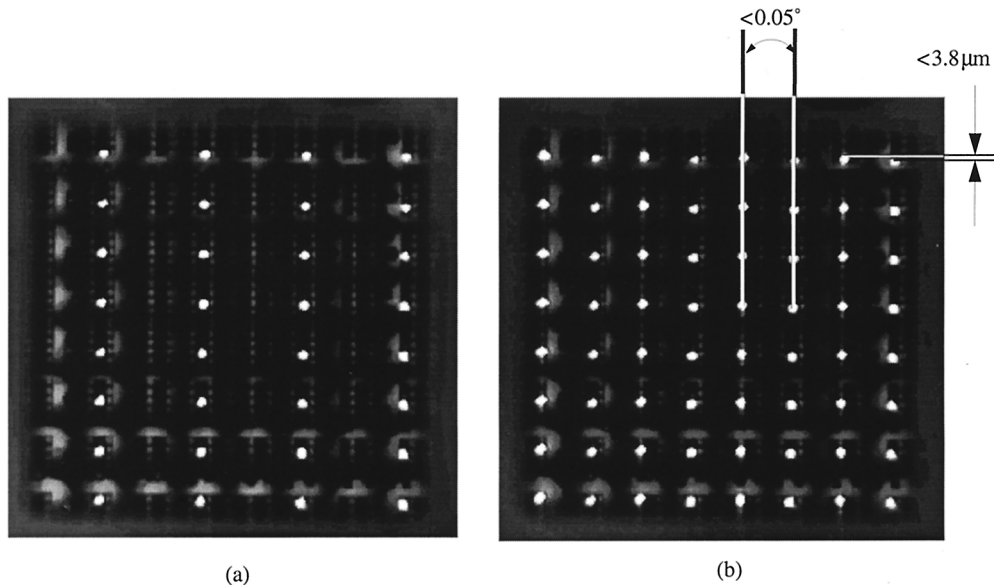


Fig. 15. Optical spots from stage_{*i*} to stage_{*i*+1}, where the bright spots are the focused signal beams and the background is the multiple images of PMMA_{*i*+1} imaged by MA_{*i*+1}. (a) Only spots from stage_{*i*} were relayed to the receiver plane of stage_{*i*+1}. (b) Optical beams from both stage_{*i*} and stage_{*i*+1} were incident on the receiver plane of stage_{*i*+1}.

16 μm away from the surface of the MA's. Figure 15 shows the focused spots from stage_{*i*} and from stage_{*i*+1} at the focal plane behind MA_{*i*+1} (the device plane of stage_{*i*+1}). The rotational error for the beams relayed from stage_{*i*} and the beams from the OPS of the stage_{*i*+1} was less than 0.05°. In addition, the positional accuracy between the beams relayed from stage_{*i*} and the beams from the OPS of the stage_{*i*+1} was examined. The offset of the optical beams relayed from stage_{*i*} was less than 3.8 μm in lateral directions away from the grid of the detector array at the stage_{*i*+1}.

B. Optical Power Uniformity

The power uniformity of the spot arrays at the PAP's and the device planes was measured. The definition used for the power uniformity across an array of beams is

$$\text{Uniformity} = 1 - \frac{P_{\max} - P_{\min}}{P_{\max} + P_{\min}}, \quad (8)$$

where P_{\max} and P_{\min} are the maximum and the minimum powers of the spots in the array, respectively.

The power uniformity of the spot array at the PAP's was measured to be 93%. After these optical beams had propagated to the modulator array planes, the uniformity of the optical beams was significantly reduced. It was found that the decrease of the power throughput was due to dust on some microlenses in the MA's. The power throughput of these dusty channels was severely degraded. If these spots were not taken into account, the power uniformity of the spot array at the modulator array plane was measured to be 92%.

For the optical beams at the detector array plane, the degraded optical beams at the modulator array

planes were further degraded since these optical beams had passed through the dust-contaminated microlenses twice. If these optical beams were ignored, the power uniformity was found to be 90% for clean interconnects. The correction of the rotational error for the 2-D array of beams, as described in Subsection 6.D, significantly increased the uniformity of the optical spots at the detector arrays.

C. Optical Power Throughput

Table 3 shows the measured collective and final power throughputs of the hybrid optical system from the optical beams at the PAP of stage_{*i*} to the detector array plane at stage_{*i*+1}. For an OPS, the main loss between the fiber input and the spot array at the PAP was the power-splitting loss of the fan-out phase grating. The power throughput was measured to be 68% ± 1% (−1.69 dB) for all spots from the fiber input to the spot array at the PAP, while the power throughput for a single optical beam was measured to be 1.7% ± 1.0% (−17.8 dB).

For the microlens relay starting from the PAP of stage_{*i*} to the modulator array plane at stage_{*i*}, the optical power throughput was measured to be 57% (−2.46 dB), which compares with the estimated measurement throughput of 75% (−1.24 dB). The 25% (−1.22-dB) additional power loss, which was within the maximum misalignment loss of 29%, as described in Subsection 3.C, included 14% (−0.67 dB) of the polarization power loss and 12% (−0.55-dB) cross-talk loss. The polarization loss is defined as the ratio of leaked power (reflected power from the PBS in the PBS+QWP assembly) to the power of the optical beams at the PAP. The loss was due to the nonlinear polarization of the optical beams into the PBS. The cross-talk loss is defined as the ratio of the total power of the nonsignal beams (the difference between

Table 3. Optical Power Throughput for Stage-to-Stage Interconnects

Components	Estimated Collective Throughput ^a (%)	Measured Collective Throughput (%)
Fiber input at stage _{<i>i</i>}	100	100
All beams at PAP _{<i>i</i>}	68	68
One beam at PAP _{<i>i</i>} (due to fan-out loss)	1.7 (-17.7 dB)	1.7 (-17.7 dB)
Micro lens at PMMA _{<i>i</i>}		
PBS+QWP (<i>T</i>) at stage _{<i>i</i>}	75 (-1.24 dB)	57 (-2.46 dB)
Micro lens at MA _{<i>i</i>}		
Diffraction effect up to transmitter plane (clipping loss, 1.3%)	99 (-0.06 dB)	
Polarization effect up to transmitter plane (worst-case polarization loss, 2.0%)	98 (-0.09 dB)	
Misalignment effect up to transmitter plane (worst-case power loss, 29.3%)	71 (-1.51 dB)	
Subtotal power TP (worst case) at transmitter plane at stage _{<i>i</i>}		
Upper bound	1.23 (-19.1 dB)	0.96 (-20.2 dB)
Lower bound	0.87 (-20.6 dB)	0.96 (-20.2 dB)
Amplitude mask ^b		
MA _{<i>i</i>}	55 (-2.56 dB)	54 (-2.7 dB)
PBS+QWP (<i>R</i>) at stage _{<i>i</i>}		
Tilt plate pair		
First macrolens	94 (-0.27 dB)	91 (-0.42 dB)
Turning mirrors	98 (-0.09 dB)	98 (-0.08 dB)
Second macrolens	94 (-0.27 dB)	94 (-0.28 dB)
Risley beam steers		
PBS+QWP (<i>R</i>) at stage _{<i>i+1</i>}		
Mirror at PMMA _{<i>i+1</i>}	79 (-1.03 dB)	66 (-1.78 dB)
PBS+QWP (<i>T</i>) at stage _{<i>i+1</i>}		
Micro lens at PMMA _{<i>i+1</i>}		
Diffraction effect from transmitter plane to receiver plane (clipping loss, 1.3%)	91 (-0.06 dB)	
Polarization effect from transmitter plane to receiver plane (worst-case of polarization loss, 6.1%)	94 (-0.27 dB)	
Misalignment effect from transmitter plane to receiver plane (worst-case power loss, 15.7%)	83 (-0.72 dB)	
Total power TP at transmitter plane at stage _{<i>i+1</i>}		
Upper bound	0.41 (-23.8 dB)	0.29 (-25.5 dB)
Lower bound	0.25 (-26.1 dB)	0.29 (-25.5 dB)

^aThe collective throughput was the collective power efficiency for a group of the optical components for which individual power throughput could not be measured in the backplane optical system.

^bIf the amplitude mask were replaced with the CMOS-SEED chip with reflectivities of the modulator array at 30% for the transmission state and 15% for the absorption state, respectively, the measured optical power throughputs at the detector array plane would be 0.13% (-28.8 dB) for the transmission state and 0.08% (-31.8 dB) for the absorption state.

the power of all the beams and the power of the signal beams) to the power of the optical beams at the PAP. The relatively large cross-talk loss might be caused by the oversized optical beams at the PAP and the inaccurate position between the OPS and the MR. Other reasons could include dust on the surfaces of the microlenses of the PMMA_{*i*} and the MA_{*i*} that scattered the incident optical beams.

The polarization loss was unexpectedly high. This might be due to the damage caused by the repeated insertion and removal of the fiber connector-physical contact connector in the OPS during system assembly. This damage changed the polarization status of the optical beams at the PAP from circular to elliptical. Other possible reasons include the AR coatings on the optical elements in the OPS that might have changed the polarization. As a result, when the extinction ratio of the optical beam at the fiber input was between 80:1 and 100:1, the ratio of the optical power at the modulator array plane to the

leaked power was measured to be between only 10:1 and 20:1.

The optical power reflected from the amplitude mask and the optical power throughput of the macrolens relay were close to the estimated values. The stage-to-stage interconnects involving turning mirrors had an approximately 1.8% (-0.08-dB) additional loss. The power throughput for signal beams to the microlens relay at stage_{*i+1*} was measured to be 66% (-1.78 dB), compared with the 79% (-1.03-dB) estimated throughput. The 16% (-0.75-dB) additional power loss included approximately 6.9% (-0.31-dB) polarization loss and 9.6% (-0.44-dB) misalignment loss, which was caused by the misalignment at the surface of the pixelated mirrors at PMMA_{*i+1*} and the microlenses at MA_{*i+1*}. The smaller polarization loss at stage_{*i+1*} might be caused by the fact that the purity of the polarization after the PBS+QWP assembly at stage_{*i*} was improved, since

the optical beams had passed through the PBS+QWP assembly twice.

The overall optical relay system had a measured total power throughput of approximately -20.2 dB (0.96%) for the optical beams from the fiber input at stage_{*i*} to the modulator array plane at stage_{*i*} and -25.5 dB (0.29%) for the optical beams from the fiber input at stage_{*i*} to the detector array plane at stage_{*i+1*}. These results show that the power throughput of the optical system is in good agreement with the predicted lower bound of the theoretical values. If the amplitude mask were replaced by the CMOS-SEED chip, the power throughput at the detector array plane would be adjusted to -28.8 dB (0.13%) for the transmission state and -31.8 dB (0.08%) for the absorption state.

8. Conclusions

The design, analysis, implementation, and characterization of a hybrid optical interconnect for a four-stage free-space optical backplane has been presented. The scalable optical system, which fitted into a 6U commercial VME electronic backplane chassis, was simple and efficient and allowed for flexible adjustment of the separation between stages. The optical system design, including the optical parameters for the hybrid relay optical system, the image mapping for a 2-D array of optical signal beams from stage to stage, alignment tolerances of the hybrid relay system, polarization-loss analysis with a Jones matrix, and the power budget, has been discussed. The implementation of the optical system, including the characterization of optical components, subsystem prealignment, and final system assembly, has been presented.

The microlens relay design involved a trade-off between the interconnection distance and the alignment tolerances. The microlens relay system with a maximum lens-to-waist configuration had the maximum interconnection distance; however, the relay system had stringent alignment tolerances. For a closed-loop multiple-stage interconnect system, the rotational error between the 2-D optical beams is an important issue. Various techniques, including *in situ* interferometric lenses built into the MA's, pairs of tilt plates, and Risley beam steerers, were used to adjust the alignment of the optical system. The alignment of the overall optical system met the initial design values. The correction of the mismatch of the 2-D array between stages was achieved with a rotational error of less than 0.05° and a lateral offset of less than $3.5 \mu\text{m}$. The polarization status of the input optical beams at the input surface (the PAP) has been found to be an important factor in determining the overall optical power throughput. The measured optical system performance was in good agreement with the lower bound of the theoretical power throughput of -20.2 dB for the optical beams from the input surface of the hybrid optical system to the modulator array and -25.5 dB to the detector array.

This research was supported by a grant from the Canadian Institute for Telecommunications Research under the National Centres for Excellence program of Canada and the Nortel/National Sciences and Engineering Research Council (Canada) Chair in Photonic Systems. In addition, D. V. Plant acknowledges support from the National Sciences and Engineering Research Council (Canada) (OGP0155159) and the Fonds pour la Formation de Chercheurs et l'Aide à la Recherche (FCAR NC-1415). The microlens arrays, PMMA's, and MA's were fabricated by M. Taghizadeh and his diffractive optics group at the Department of Physics, Heriot-Watt University, Edinburgh, Scotland. The multiple-phase gratings were obtained from the Advanced Research Projects Agency-sponsored Consortium for Optical and Optoelectronic Technologies for Computing conducted by George Mason University and the Honeywell Technology Center in 1996.

References

1. J. W. Goodman, F. I. Leonberger, S. Y. Kung, and R. A. Athale, "Optical interconnects for VLSI systems," *Proc. IEEE* **72**, 850–875 (1984).
2. T. Sakano, T. Matsumoto, K. Noguchi, and T. Sawabe, "Design and performance of a multiprocessor system employing board-to-board free-space optical interconnects: COSINE-1," *Appl. Opt.* **30**, 2334–2343 (1991).
3. F. B. McCormick, T. J. Cloonan, F. A. P. Tooley, A. L. Lentine, J. M. Sasian, J. L. Brubaker, R. L. Morrison, S. L. Walker, R. J. Crisci, R. A. Novotny, S. J. Hinterlong, H. S. Hinton, and E. Kerbis, "Six-stage digital free-space optical switching network using symmetric self-electro-optic-effect devices," *Appl. Opt.* **32**, 5153–5171 (1993).
4. F. B. McCormick, T. J. Cloonan, A. L. Lentine, J. M. Sasian, R. L. Morrison, M. G. Beckman, S. L. Walker, M. J. Wojcik, S. J. Hinterlong, R. J. Crisci, R. A. Novotny, and H. S. Hinton, "Five-stage free-space optical switching network with field-effect transistor self-electro-optic-effect smart-pixel arrays," *Appl. Opt.* **33**, 1601–1618 (1994).
5. G. F. Sauter, "Gradient-index lens optical backplane," *Appl. Opt.* **33**, 3446–3453 (1994).
6. T. Sakano, T. Matsumoto, and K. Noguchi, "Three-dimensional board-to-board free-space optical interconnects and their application to the prototype multiprocessor system: COSINE-III," *Appl. Opt.* **34**, 1815–1822 (1995).
7. T. Sakano, K. Kimura, K. Noguchi, and N. Naito, " 256×256 turn-over-type free-space multichannel optical switch based on polarization control using liquid-crystal spatial light modulators," *Appl. Opt.* **34**, 2581–2589 (1995).
8. S. Araki, M. Kajita, K. Kasahara, K. Kubota, K. Kurihara, I. Redmond, E. Schenfeld, and T. Suzuki, "Experimental free-space optical network for massively computers," *Appl. Opt.* **35**, 1269–1281 (1996).
9. D. V. Plant, B. Robertson, H. S. Hinton, M. H. Ayliffe, G. C. Boisset, W. Hsiao, D. Kabal, N. K. Kim, Y. S. Liu, M. R. Otazo, D. Pavlasek, A. Z. Shang, J. Simmons, K. Song, D. A. Thompson, and W. M. Robertson, " 4×4 vertical-cavity-surface-emitting laser (VCSEL) and metal-semiconductor-metal (MSM) optical backplane demonstrator system," *Appl. Opt.* **35**, 6365–6368 (1996).
10. B. Kelly, P. Horan, F. A. P. Tooley, M. R. Taghizadeh, and J. Hegarty, "Optically lateral inhibition networks that use self-linearized self-electro-optic-effect devices: theory and experiment," *Appl. Opt.* **35**, 1372–1380 (1996).
11. T. H. Szymanski and H. S. Hinton, "Reconfigurable intelligent

- optical backplane for parallel computing and communications," *Appl. Opt.* **35**, 1253–1268 (1996).
12. B. Supmonchai and T. H. Szymanski, "High speed VLSI concentrators for terabit intelligent optical backplanes," paper to be presented at the International Conference on Optical Computing, Brugge, Belgium, 17–20 June 1998.
 13. T. H. Szymanski and H. S. Hinton, "Architecture of a terabit free-space intelligent optical backplane," *J. Parallel Distr. Comput.* (to be published).
 14. F. A. P. Tooley, "Challenges in optically interconnecting electronics," *IEEE J. Sel. Top. Quantum Electron.* **2**, 3–13 (1996).
 15. D. V. Plant, B. Robertson, H. S. Hinton, M. H. Ayliffe, G. C. Boisset, D. J. Goodwill, D. Kabal, R. Iyer, Y. S. Liu, D. R. Rolston, M. Venditti, T. H. Szymanski, W. W. Robertson, and M. R. Taghizadeh, "Optical, optomechanical, and optoelectronic design and operational testing of a multistage optical backplane demonstration system," in *Proceedings of the Third International Conference on Massively Parallel Processing and Optical Interconnections*, A. Gottlieb, Y. Li, and E. Schenfeld, eds. (IEEE, Piscataway, N.J., 1996), pp. 306–312.
 16. A. W. Lohmann, "Image formation of dilute arrays for optical information processing," *Opt. Commun.* **86**, 365–370 (1986).
 17. N. C. Craft and A. Y. Feldblum, "Optical interconnects based on arrays of surface-emitting lasers and lenslets," *Appl. Opt.* **31**, 1735–1739 (1992).
 18. K. Tanaka and O. Kanzaki, "Focus of a diffracted Gaussian beam through a finite aperture lens: experimental and numerical investigations," *Appl. Opt.* **26**, 390–395 (1987).
 19. F. B. McCormick, F. A. P. Tooley, T. J. Cloonan, J. M. Sasian, H. S. Hinton, K. O. Merserau, and A. Y. Feldblum, "Optical interconnections using microlens arrays," *Opt. Quantum Electron.* **24**, S465–S477 (1992).
 20. B. Robertson, G. C. Boisset, H. S. Hinton, Y. S. Liu, N. H. Kim, M. R. Otazo, D. Pavlasek, D. V. Plant, D. Rolston, and V. M. Robertson, "Design of a lenslet array based free-space optical backplane demonstrator," presented at the International Conference on Optical Computing, 22–25 August 1994, Edinburgh, UK.
 21. D. Rolston, B. Robertson, D. V. Plant, and H. S. Hinton, "Analysis of a microchannel interconnect based on the clustering of smart-pixel-device windows," *Appl. Opt.* **35**, 1220–1233 (1996).
 22. D. Kabal, M. H. Ayliffe, G. C. Boisset, D. V. Plant, D. R. Rolston, and M. B. Venditti, "Packaging of two-dimensional smart pixel arrays," presented at the IEEE/Leos 1996 Summer Topical Meeting on Advanced Applications of Lasers in Materials and Processing, 5–9 August 1996, Keystone, Col.
 23. R. Iyer, Y. S. Liu, G. C. Boisset, D. J. Goodwill, M. H. Ayliffe, B. Robertson, W. M. Robertson, D. Kabal, F. Lacroix, and D. V. Plant, "Design, implementation, and characterization of an optical power supply spot-array generator for a four-stage free-space optical backplane," *Appl. Opt.* **36**, 9230–9242 (1997).
 24. G. C. Boisset, M. H. Ayliffe, B. Robertson, R. Iyer, Y. S. Liu, D. V. Plant, D. J. Goodwill, D. Kabal, and D. Pavlasek, "Optomechanics for a four-stage hybrid-self-electro-optic-effect-device-based free-space optical backplane," *Appl. Opt.* **36**, 7341–7358 (1997).
 25. S. M. Prince, C. P. Beauchamp, and F. A. P. Tooley, "Tolerancing of array of microlens relays: a case study," *J. Eur. Opt. Soc. A* **3**, 151–156 (1994).
 26. Y. S. Liu, B. Robertson, D. V. Plant, H. S. Hinton, and W. M. Robertson, "Design and characterization of a microchannel optical interconnect for optical backplanes," *Appl. Opt.* **34**, 3127–3141 (1997).
 27. S. A. Self, "Focusing of spherical Gaussian beams," *Appl. Opt.* **22**, 658–661 (1983).
 28. P. Belland and J. P. Crenn, "Changes in the characteristics of a Gaussian beam weakly diffracted by a circular aperture," *Appl. Opt.* **21**, 522–527 (1982).
 29. K. Hamanaka, "Optical bus interconnection system using Selfoc lenses," *Opt. Lett.* **16**, 1222–1224 (1991).
 30. B. Robertson, Y. S. Liu, G. C. Boisset, M. R. Taghizadeh, and D. V. Plant, "*In situ* interferometric alignment systems for the assembly of microchannel relay systems," *Appl. Opt.* **36**, 9253–9260 (1997).
 31. Sinclair Optics, Inc., 6780 Palmyra Road, Fairport, New York 14450.
 32. H. Sasaki, K. Shinozaki, and T. Kamijoh, "Reduced alignment accuracy requirement using focused Gaussian beams for free-space optical interconnection," *Opt. Eng.* **35**, 1550–1560 (1996).
 33. Y. S. Liu, "Design, implementation, and characterization of free-space optical interconnects for optical backplanes," Ph.D. dissertation (McGill University, Montreal, Quebec, Canada, 1997), Chap. 3.
 34. A. R. Al-Rashed and B. E. A. Saleh, "Decentered Gaussian beams," *Appl. Opt.* **34**, 6819–6825 (1995).
 35. J. Jahns and S. J. Walker, "Two-dimensional array of diffractive microlenses fabricated by thin film deposition," *Appl. Opt.* **29**, 931–936 (1990).
 36. G. L. Yip, P. C. Noutsios, and L. Chen, "Improved propagation-mode near-field method for refractive-index profiling of optical waveguides," *Appl. Opt.* **35**, 2060–2068 (1996).